Spontaneous cell internalization of a spatially-confined proliferating blastomere: A mechanical interpretation on worm gastrulation

Jiao Miao[1†*], Guoye Guan[1†], Chao Tang[1,2,3*]

1. Center for Quantitative Biology, Peking University, Beijing 100871, China

2. Peking-Tsinghua Center for Life Sciences, Peking University, Beijing 100871, China

3. School of Physics, Peking University, Beijing 100871, China

* For correspondence: jiaomiao@pku.edu.cn (JM); tangc@pku.edu.cn (CT)

† These authors contributed equally to this work.

ABSTRACT

Cell internalization of a blastomere, namely gastrulation, is a common and significant milestone during development of metazoans from worm to human, which generates multiple embryonic layers with distinct cell fates and spatial organizations. Although many molecular activities (e.g., cell polarization, asymmetrical intercellular adhesion, and apical actomyosin cortex contraction) have been revealed to facilitate this morphogenetic process, in this paper, we focus on gastrulation of the worm *Caenorhabditis elegans* and demonstrate that even a simple mechanical system, like a group of cells with isotropic repulsive and attractive interactions, can experience such internalization behavior spontaneously when dividing within a confined space. In principle, when the total cell number exceeds a threshold, a double-layer structure acquires lower potential energy and longer neighbor distance than the single-layer one. Besides, both mechanical analysis and simulation suggest that the cells with a large size or placed near a small-curvature boundary are easier to internalize. Last but not least, extra regulation on a limited part of cells to internalize autonomously can stabilize this process against motional noise. Our work successfully recaptures many key characteristics in worm gastrulation by mechanical modeling and provides a novel and rational interpretation on how this phenomenon emerges and is optimally programed.

INTRODUCTION

Metazoan embryogenesis starts from a single fertilized zygote and ends into a vast number of cells with accurate spatial patterns and fate specifications (***Dehaan and Ebert, 1964***; ***Kumar et al., 2015***; ***Farrell et al., 2018***; ***Packer et al., 2019***). Those cells constitute multiple types of tissues and organs in an animal, such as intestine, muscle, and skin, which need precise and robust control on both morphogenesis and differentiation. During the rapid cleavage of blastomere, a dynamic process called gastrulation would be activated at specific timing to reposition the cells into different germ layers, usually including endoderm, mesoderm, and ectoderm (***Stern, 2004***; ***Solnica-Krezel and Sepich, 2012***). Geometrically, all the cells are initially located adjacent to the inner side of shell like a 2-dimensional surface, then they partially internalize to form different layers. Although the molecular mechanism and the proportion of cells that move inward vary from species to species, this morphological change is common among all kinds of multicellular animals, including but not limited to nematode, ascidian, fly, frog, fish, chick, mouse and human (***Houthoofd et al., 2006***; ***Swalla, 1993***; ***Lemke et al., 2015***; ***Heasman, 2006***; ***Rohde and Heisenberg, 2007***; ***Chapman et al., 2002***; ***Tam and Behringer, 1997***; ***Ghimire et al., 2021***). As the developmental biologist Lewis Wolpert said, "not birth, marriage or death, but gastrulation which is truly the most important time in your life" (***Vicente, 2015***; ***Illman, 2021***).

The eutelic nematode *Caenorhabditis elegans* (hereafter referred to as *C. elegans*) is a type of tiny transparent worm, which is famous for its highly invariant developmental programs at the cellular level and eventually generates 558 non-identical and tracible cells in a hatched larva (***Sulston et al., 1983***). Thus, it has been one of the most popular model animals for developmental biology, and a lot of molecular regulations on gastrulation have been unraveled using this system (***Corsi et al., 2015***; ***Nance et al., 2005***; ***Goldstein and Nance, 2020***). During *C. elegans* embryogenesis, the gastrulating movements last for

a long period (from 26- to ~300-cell stage) and the cells from different lineages internalize group by group (roughly following an order as E → P4 → MS → D → C → AB) (***Chisholm and Hardin, 2005***; ***Nance and Priess, 2002***). ***Figure 1A*** shows the *C. elegans* embryonic development from 4- to 350-cell stage imaged by 3-dimensional time-lapse confocal microscopy, which could provide quantitative information of each cell's nucleus position (GFP-labelled) and membrane morphology (mCherry-labelled) (***Cao et al., 2020***). Prior to gastrulation onset, all cells are in contact with the shell (***Nance and Priess, 2002***). At 26- to 28-cell stage, gastrulation is activated and the two gut precursor cells, Ea and Ep in E lineage, together migrate inward by their lateral adhesion to neighbor cells and apical contraction at outer surface (***Marston et al., 2016***). At 44-cell stage (right before E2 divisions), those motions lead to a stratified multicellular structure consisting of E2 cells inside and the others outside, which is highly reproducible among individual embryos with single-cell accuracy (***Figure 1B***). Using the segmented cell morphology of 17 *C. elegans* wild-type embryo samples collected in our previous work (***Cao et al., 2020***), an approximation on the total number of internal cells (without contact to the outer space) shows that the first fully internalization occurs at 42- to 46-cell stage and the internal cells can make up around 18 ± 1% of the total cell number of the embryo at ~350-cell stage (***Figure 1C-D*** and ***Table S1***). Even though many molecular regulations that facilitate this morphogenetic process have been uncovered in all kinds of organisms, a comprehensive mechanical interpretation on such general phenomenon (hereafter referred to as cell internalization), especially for its emergence and optimization principle/strategy, is still in lack. Moreover, little is known about how the elementary physical factors (e.g., stiffness and adhesion of cells) coordinate the internalization behavior, for example, to control the activation timing and total number of internalizing cells with precision and robustness.

In this paper, we first establish a standard computational pipeline to simulate *C. elegans* morphogenesis from 4- to 330-cell stage, using a simplified coarse-grained model. Then we demonstrate that cell internalization would emerge spontaneously in all conditions of physical parameter setting. We then systematically investigate how different factors affect the cell internalization, including stiffness and adhesion of cells, cell size and cell position. This morphogenetic process becomes less reproducible when the system is suffering motional noise, which however can be stabilized by adding active force on specific cells to drive their ingression. Our work proposes a computational framework to study cell internalization, reveals the mechanical essence of worm gastrulation and provides new insight into its control principle/strategy.

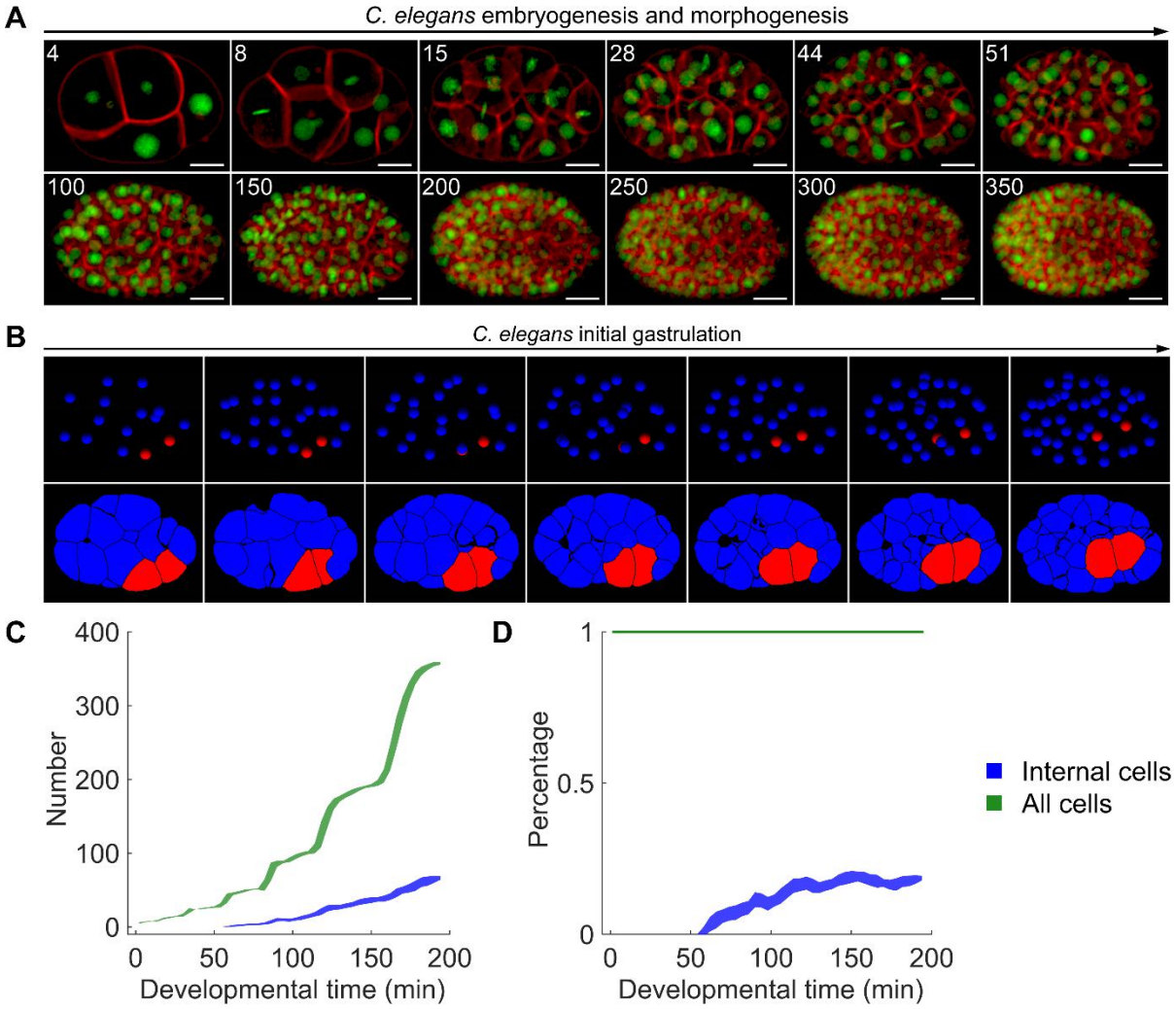

Figure 1. The cell internalization during *C. elegans* early development (data obtained from *Cao et al., 2020*). (A) *C. elegans* embryogenesis and morphogenesis imaged by 3-dimensional time-lapse confocal microscopy; green fluorescence, cell nuclei labelled by GFP; red fluorescence, cell membranes labelled by mCherry; from top left to bottom right, image projection along the shooting direction when the total cell number = 4 (before AB2 divisions), 8 (before P2 division), 15 (before AB8 and P3 divisions), 28 (before AB16 divisions), 44 (before E2 divisions), 51 (before C4 divisions), ~100, ~150, ~200, ~250, ~300 and ~350, which are denoted on the top left of each subgraph; scale bar, 10 μm. (B) Cell tracing and membrane segmentation (cross-section image of a specific focal plane) at selected time points for illustrating the initial gastrulation; the 1st row, nucleus tracing results; the 2nd row, membrane segmentation results; the internal between consecutive images is 4 time points ≈ 5.6 min; the gut precursor cells E2 and the other cells are colored in red and blue respectively. (C, D) An approximation on the (C) number and (D) percentage of all cells and internal cells over time using 17 wild-type embryo samples recorded from 4- to 350-cell stage; the painted region represents the data distribution by MEAN ± STD; the starting point of developmental time is set by the last moment of 4-cell stage; blue, internal cells without contact to the outer space; green, all cells with detected nucleus.

RESULTS

A computational pipeline based on coarse-grained model is established for simulating cell-cell interactions, cell divisions and cell motions within a confined space.

To interpret the cell internalization phenomenon that is widely found in the animal kingdom, we start from building up a mechanics-based computational pipeline to simulate cell-cell interactions and cell motions within a confined space. A coarse-grained model, in which cells are simplified as particles and subject to distance-dependent repulsion and attraction from their

neighbors and repulsion from the shell, has been proposed to be capable to produce the multicellular structures that resemble the ones observed in live *C. elegans* embryo (***Figure 2A-B***) (***Fickentscher et al., 2013***; ***Fickentscher et al., 2016***; ***Yamamoto and Kimura, 2017***; ***Tian et al., 2020***; ***Guan et al., 2020***). In the model, the cell motion is constrained inside an ellipsoidal shell which is axisymmetric about its anterior-posterior axis, namely the major axis along x (***Figure 2C***). Cell divisions are tangential to the shell and approximately oriented along the anterior-posterior axis, with an exception that the ABa and ABp cells divide along the left-right axis, namely the minor axis along y (***Figure 2D*** and see ***Materials and Methods***) (***Sugioka and Bowerman, 2018***). The mechanical parameters have been well-tuned in our previous work, which can reproduce the embryo structures at 4-, 8-, 12-, 26- and 51-cell stages (***Guan et al., 2020***). Other parameters such as cell volume segregation ratio and shell size are assigned with the values measured by *in vivo* experiments, and detailed in ***Materials and Methods***. The simulation starts from the rhombic 4-cell structure and proceeds according to the highly conserved cell division sequence recorded experimentally until reaching 330 cells (***Table S2***) (***Guan et al., 2019***). Such a simplified model is expected to capture the most fundamental features and rules that govern the multibody mechanical system.

Cell internalization always takes place spontaneously in all conditions of physical parameter setting.

At first, the system is noise-free and set to resemble the developmental manners in *C. elegans* embryo (repulsive factor $K = 0.01$ and attractive factor $\alpha = 0.9$; Condition 1). A cell in E lineage first moves toward the embryo center from the periphery of blastomere when the total cell number reaches 46, followed by more and more cells internalizing and accumulated internally (***Figure 2E-F***, ***Table 3***, and ***Video 1-2***). Intriguingly, the developmental stage when initial cell internalization occurs is close to the one in a real embryo (i.e., the E2 cells start ingressing at 26- to 28-cell stage, settle and divide at 44-cell stage, afterwards the blastomere reaches 46 cells) (***Figure 1B***) (***Nance and Priess, 2002***; ***Nance et al., 2005***). To achieve a more fundamental understanding on cell internalization, we next consider 5 more conditions with different physical parameters settings, by changing the attractive force, division asymmetry, division orientation and division sequence from the abovementioned experiment-based default into the simplest case (i.e., without attractive force, and with symmetric division whose orientation and sequence are fully randomized). Regarding the conditions with stochasticity, a total of 100 independent repeats are generated for each and their mean behavior would be used for subsequent comparison. Surprisingly, cell internalization emerges in all the conditions at activation timing (i.e., cell stage) varying from 44 to 87, indicating the spontaneity of such phenomenon and its independence on the physical parameters considered here (***Figure 2G-H*** and ***Table 3***).

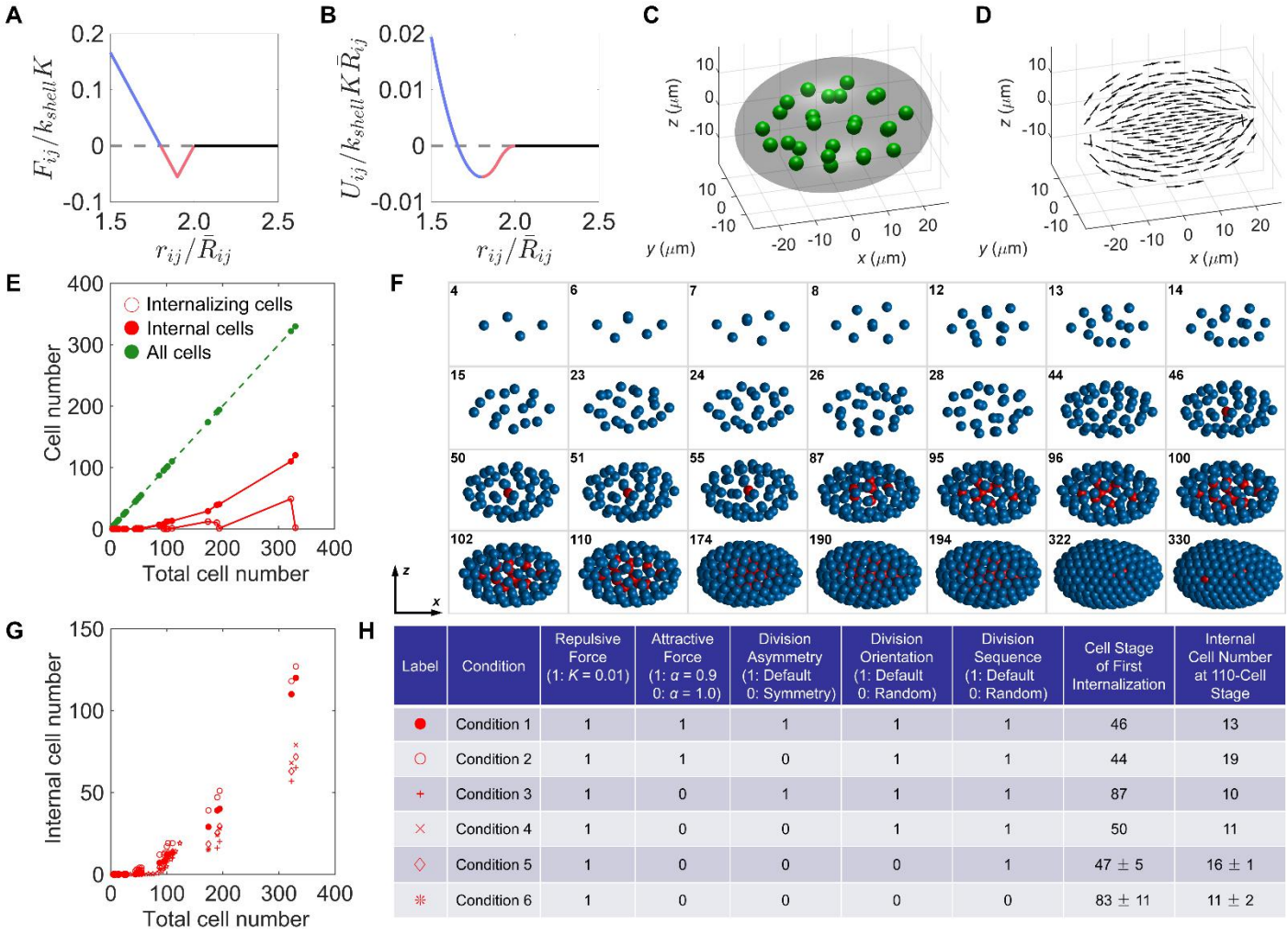

Label	Condition	Repulsive Force (1: K = 0.01)	Attractive Force (1: α = 0.9 0: α = 1.0)	Division Asymmetry (1: Default 0: Symmetry)	Division Orientation (1: Default 0: Random)	Division Sequence (1: Default 0: Random)	Cell Stage of First Internalization	Internal Cell Number at 110-Cell Stage
●	Condition 1	1	1	1	1	1	46	13
○	Condition 2	1	1	0	1	1	44	19
+	Condition 3	1	0	1	1	1	87	10
×	Condition 4	1	0	0	1	1	50	11
◇	Condition 5	1	0	0	0	1	47 ± 5	16 ± 1
❋	Condition 6	1	0	0	0	0	83 ± 11	11 ± 2

Figure 2. The simulation on *C. elegans* early embryogenesis and morphogenesis. (A, B) Schematics of dimensionless (A) force $\frac{F_{ij}}{k_{shell}K}$ and (B) potential $\frac{U_{ij}}{k_{shell}K\bar{R}_{ij}}$ between cells, which rely on the dimensionless cell-to-cell distance $\frac{r_{ij}}{\bar{R}_{ij}}$ (i and j represent two cells' identity labels; F_{ij}, U_{ij} and r_{ij} represent the original force, potential and distance between two cells, respectively; k_{shell} and K represent the stiffness of the shell and the cell, respectively; $\bar{R}_{ij}$ represents the average of two cells' radii); blue line, repulsion when $\frac{r_{ij}}{\bar{R}_{ij}} < 2\alpha$; red line, attraction when $2\alpha \leq \frac{r_{ij}}{\bar{R}_{ij}} < 2$; black line, no interaction when $\frac{r_{ij}}{\bar{R}_{ij}} \geq 2$. (C) Schamatic of cells placed inside an ellipsoidal shell in mechanical equilibrium; green sphere, cells; gray shadow, shell. (D) Schematic of cell division orientation tangential to the shell and approximately oriented along the anterior-posterior axis (see ***Materials and Methods***); the arrow denotes the prescribed division orientation at a specific position. (E) Number of internalizing cells and internal cells over the increase of total cell number; red empty circle, internalizing cells; red solid circle, internal cells; green solid circle, all cells. (F) Simulated embryo structure from 4- to 330-cell stage (from top left to bottom right); the total cell number is denoted on the top left of each subgraph; the cells with and without contact to the shell are colored in blue and red respectively. (G, H) Number of internal cells over the increase of total cell number when the physical parameter settings are different; the 6 conditions and corresponding symbols and settings are listed in (H).

Cell internalization can reduce a blastomere's systematic potential energy by redistributing the cell positions more sparsely.

Since the emergence of cell internalization relies little on a few of physical parameter settings (***Figure 2G***), next we seek to to unveil the most basic mechanisms of this phenomenon. Here we introduce a phenomenological model, which is further simplified as 2-dimensional (2D) and combines an oval-shaped shell and N cells inside. Those cells have area equally divided from the shell's area, and interact with each other only through repulsion (K = 0.01 and α = 1); they are placed internally

tangent to the boundary and have totally same distance to their neighbors. Then we construct the single-layer structure (with N cells contacting the boundary) and double-layer structure (with N-1 cells contacting the boundary and 1 cell at the center) to represent the topological change before and after cell internalization (***Figure 3A***). Interestingly, when the total cell number is smaller, the double-layer structure has larger system potential energy and shorter average neighbor distance than the ones of single-layer structure (***Figure 3B-C***). This relationship changes as the total cell number grows, which explains why the *in silico* blastomere tends to be single-layer in the beginning and double-layer in the end. In the simulation with experimental parameters, the first cell internalization roughly proceeds between time points $10^4 \sim 10^5$, also accompanied by decrease in system potential energy and increase in average neighbor distance, supporting the explanation that the cells are repositioned sparsely and the system releases potential energy by cell internalization (***Figure 3D-E*** and ***Table S4***).

Cell internalization is primarily driven by cell-cell repulsion but not attraction.

Using the phenomenological model, we perform force analysis onto the cell which contacts with two neighbor cells and a curved boundary. At an initial state, the resultant force imposed on the cell by its neighbors is oriented towards the shell due to the curvature. A restoring force could exist when the cell's position is perturbed, making it stably contact the shell with pressure (***Figure 3F***). When the perturbation is strong enough and makes the cell more distant to the shell, the resultant force from neighbors would turn to be oriented inward and no restoring force remains. Therefore, a cell would keep ingressing irreversibly once it leaves the position of equilibrium. To validate the hypothesis that cell-cell repulsion is key for a cell to internalize, we utilize the the simulation with experimental parameters and eliminate the attractive force between the first internalizing cell and its neighbors. This modification results in internalization of the same cell, and similar patterns in system potential energy and average neighbor distance, supporting the repulsive force as the key of cell internalization instead of attractive force (***Figure 3D-E***, ***Figure S1*** and ***Table S4***).

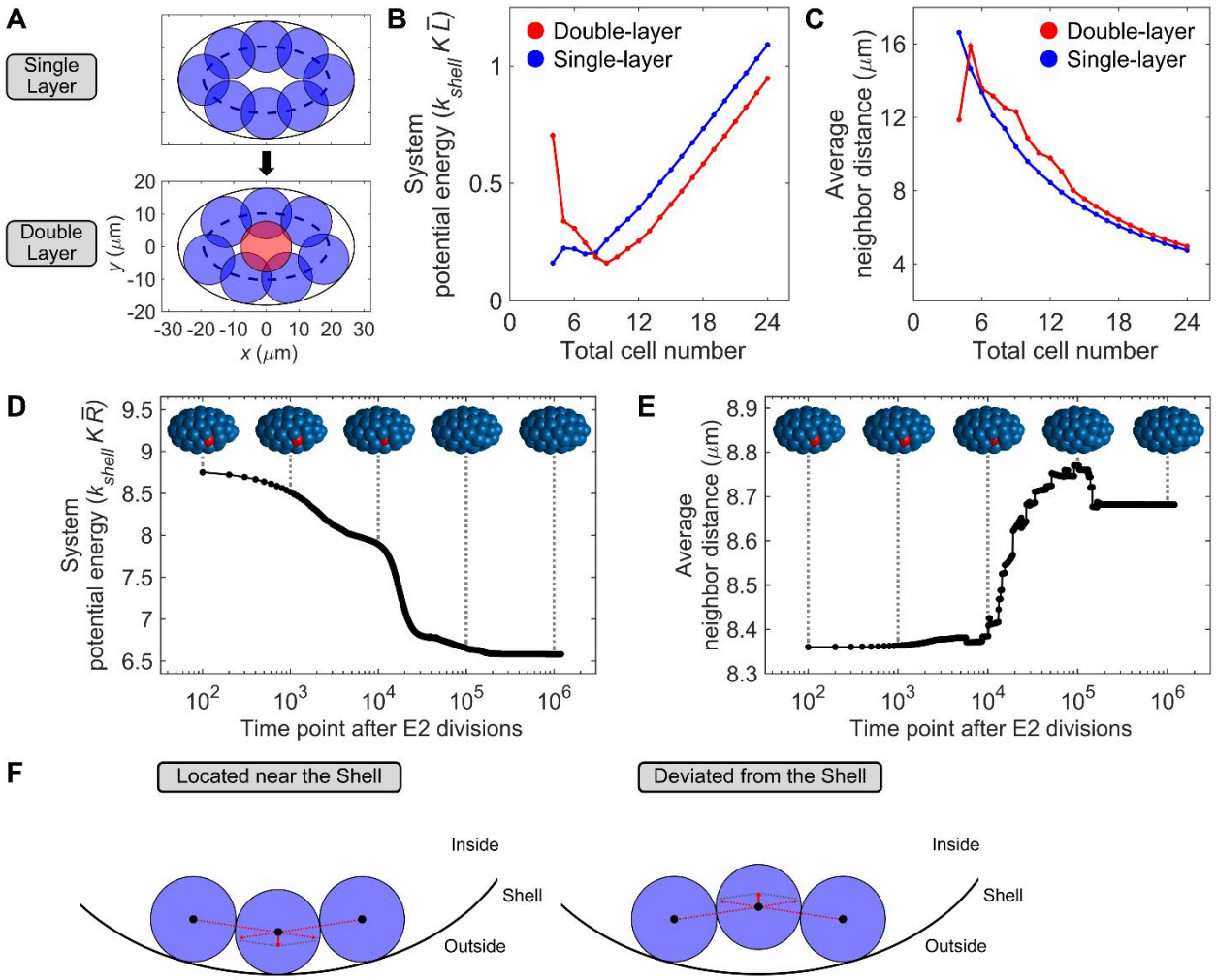

Figure 3. The mechanical explanation on cell internalization. (A) A 2-dimensional system combining an elliptical shell (long diameter $2L_x = 2 \times 27$ μm, short diameter $2L_y = 2 \times 18$ μm) and N cells with equal area (radius $\overline{R} = \sqrt{\frac{L_x L_y}{N}}$); the single-layer and double-layer structures are illustrated on top the bottom respectively; the cells with and without contact to the shell are colored in blue and red respectively. (B) The change of system potential energy as the total cell number grows in the 2D system; $\overline{L} = \sqrt{L_x L_y}$ is the equivalent radius of the circle with same area to the elliptical shell. (C) The change of average neighbor distance as the total cell number grows in the 2D system. (D, E) The temporal change of (D) system potential energy and (E) average neighbor distance in the simulation with experimental parameters when the first cell internalization proceeds (46-cell stage); the embryo structures at time points 10^2, 10^3, 10^4, 10^5 and 10^6 are illustrated on top, with the internalizing cell painted in red and the others painted in blue. (F) The resultant force imposed on a specific cell by its two neighbors when it is located near the shell (left) or deviated from the shell (right); the component and resultant repulsive forces are illustrated by solid and dashed arrows respectively.

In consideration of the force field combining both repulsion and attraction, the attraction, which mainly origins from adhesive proteins and gap junctions, neutralizes a part of the cytoskeleton-associated repulsion all across the effective range $0 < \frac{r_{ij}}{\overline{R}_{ij}} < 2$, and changes the cell-to-cell distance in mechanical equilibrium from $r_{ij} = 2\overline{R}_{ij}$ to $r_{ij} = \alpha \cdot 2\overline{R}_{ij}$ (***Figure 4A-B***) (***Marston et al., 2016***; ***Simonsen et al., 2014***; ***Pegoraro et al., 2017***; ***Yamamoto and Kimura, 2017***). Therefore, the attraction would weaken the outward-oriented repulsive force on a cell and increase the chance of cell internalization, while repulsion has opposite effect. To verify this idea, we add motional noise into the simulation with experimental parameters, and tune the repulsive and attractive strengths respectively ($\eta = 10^{-4} \sim 10^{-2}$, $K_R = 10^{-3} \sim 10^{-1}$, $K_A = 10^{-3} \sim 10^{-1}$, repeat number =

50) (*Figure 4C*). K_R and K_A is defined as the slope of $\frac{F_{ij}}{k_{shell}K} - \frac{r_{ij}}{\bar{R}_{ij}}$ curve with respect to the repulsive range $\frac{r_{ij}}{\bar{R}_{ij}} < 2\alpha$ and attractive range $2\alpha \leq \frac{r_{ij}}{\bar{R}_{ij}} < 2$, respectively, meanwhile the curve has a fixed point on $\frac{r_{ij}}{\bar{R}_{ij}} = 2\alpha$ (*Figure 4D*). As expected, the activation timing (i.e., total cell number) of the first cell internalization is positively correlated to the repulsive strength and negatively correlated to the attractive strength, suggesting that the repulsive and attractive force can inhibit and enhance the trend of cell internalization respectively (*Figure 4D-E* and *Table S5*).

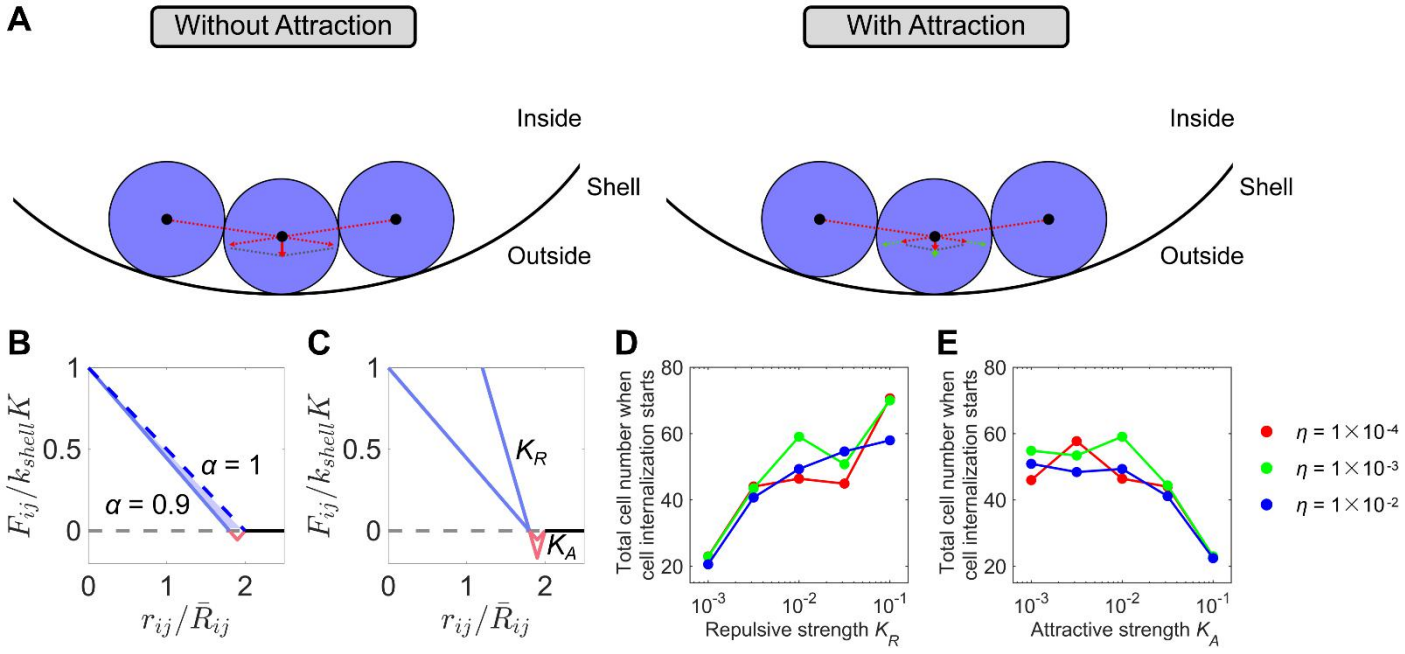

Figure 4. The effect of cell-cell attraction on cell internalization. (A) The resultant force imposed a specific cell by its two neighbors when there's only repulsive force (left) or both repulsive and attractive force (right); the component and resultant forces are illustrated by solid and dashed arrows respectively; red, repulsive force; green, attractive force. (B) Schematics of dimensionless force $\frac{F_{ij}}{k_{shell}K}$ between cells; solid line, force field consisting of both repulsion and attraction (α = 0.9); dashed line, force field consisting of only repulsion (α = 1); the repulsion neutralized by attraction is highlighted by blue shade. (C) Schematics of dimensionless force $\frac{F_{ij}}{k_{shell}K}$ between cells when the repulsive strength K_R and attractive strength K_A vary from 10^{-3} to 10^{-1}. The meanings of coefficient and color in (B, C) are totally same to the ones in *Figure 2A*. (D, E) The total cell number when cell internalization starts under different assigned values on (D) repulsive strength and (E) attractive strength; the relationship between colors and noise amplitudes is denoted on right.

The cells with a large size or placed near a small-curvature boundary have a relatively higher probability to internalize.

Here, we explore what kind of cells are easier to internalize. For simplicity, we combine the 2D phenomenological model and the mechanical simulation with only intercellular repulsion, symmetric division and randomized division orientation and sequence (Condition 6, *Figure 2H*). The simplest scenes can clear up the effect of most factors, and help search the elementary rules on cell internalization.

First, when a cell has a significantly larger size than its two neighbors, the direction of the resultant force imposed on it could change from outward to inward (*Figure 5A*). In the simulation, as the cells are programed to divide equally round by round, there are only two kinds of cells with different sizes (the larger has volume twice of the smaller). Hence, we classify the cells into "larger cells" and "smaller cells" from 1- to 128-cell stage; if the total cell number is the power of 2, the data is excluded because all the cells are homogeneous. The simulation (repeat number = 100) shows that the larger cells indeed have higher probability of cell internalization than the smaller cells (*Figure 5B*). Fascinatingly, in the real *C. elegans* embryo, the

first internalizing cells, E2, acquire the largest volume among all cells by postponing their divisions, which is induced by tissue-specific zygotic transcription and gap phase introduction (*Wong et al., 2016*) (*Figure 5C-D*).

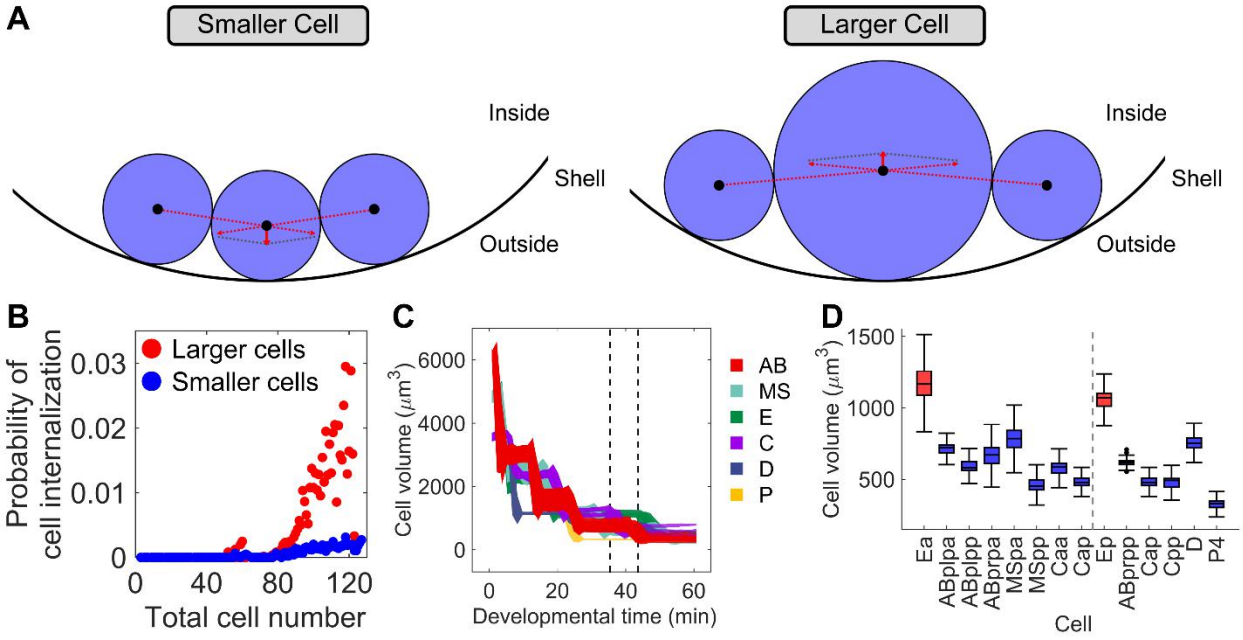

Figure 5. The effect of cell size on cell internalization. (A) The resultant force imposed a specific cell by its two neighbors when it has a relatively smaller (left) or larger size (right); the component and resultant repulsive forces are illustrated by solid and dashed arrows respectively. (B) Probability of cell internalization in the simulation with only intercellular repulsion, symmetric division and randomized division orientation and sequence; red points, larger cells; blue points, smaller cells. (C) Change of cell volume in different cell types over developmental time; the starting point of developmental time is set by the last moment of 4-cell stage; the start and end of the first cell internalization, namely 26- to 44-cell stage, is denoted by black dashed lines; the relationship between colors and cell types is denoted on right. (D) Cell volume of E2 cells and their neighbors at 28-cell stage; left panel, Ea cell and its neighbors; right panel, Ep cell and its neighbors. The measurements in (C, D) are performed using the data of 17 segmented embryos collected in *Cao et al., 2020*.

Secondly, when a cell is placed near the boundary with a smaller curvature, the forces imposed on it by its similar sized neighbors would have less weight outward (*Figure 6A*). For the ellipsoidal shell, the curvature is small in the middle and large on both sides, suggesting that the cells around the center are easier to internalize. In the simulation, distributions of both the larger and smaller internalizing cells approximately obey the bell shape, supporting our hypothesis (*Figure 6B-C*). In the real *C. elegans* embryo, a total of 66 cells were proposed to gastrulate before (*Harrell and Goldstein, 2011*), among which 32 cells have full lifespan continuously recorded in *Cao et al., 2020*. Here, we take an average of a cell's positions at its first and last time points to approximate its internalizing position (*Table S1*) . Regarding the 32 cells, the 1/3 outermost region (x > 18 μm or x < -18 μm) contains less than 8% data, while the 1/2 central region (-13.5 μm < x < 13.5 μm) contains over 74% data (*Figure 6D*). The bell shape calculated with real cells is obviously wider than the ones in simulation, implying that other unknown cues may affect the cell internalization programs as well. The different shell shape between *in silico* and *in vivo* may be a reason, but needs further verification.

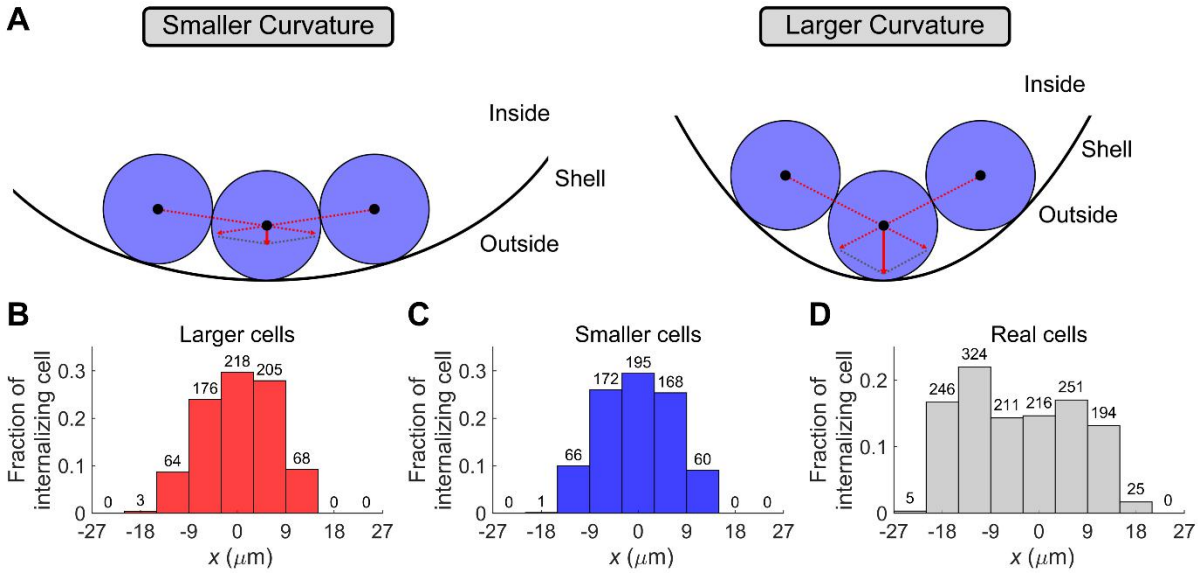

Figure 6. The effect of shell curvature on cell internalization. (A) The resultant force imposed on a specific cell by its two neighbors when placed near a smaller-curvature (left) or larger-curvature boundary (right); the component and resultant repulsive forces are illustrated by solid and dashed arrows respectively. (B, C) Fraction of internalizing cell of the (B) larger and (C) smaller cells in the simulation with only intercellular repulsion and randomized division; the internalizing cell number in each region is labeled on the top of the column. (D) Fraction of internalizing cell in the real system; the internalizing cell number in each region is labeled on the top of the column.

Cell internalization behaviors could be disturbed by motional noise and stabilized by regulatory active force imposed on specific cells to direct their inward movements.

During metazoan gastrulation, the activation timing and cell types that move inward are crucial and accurate, because those cells with specific fates must play their irreplaceable roles after internalization, for instance, generating the endoderm or mesoderm of gastrula. However, the motional noise always exists during embryogenesis (*Li et al., 2018*; *Guan et al., 2019*), which brings variability in the cell positions among individuals and is harmful for the stereotypic developmental programs, such as the location and communication of specific cells (*Sulston et al., 1983*; *Eisenmann, 2005*; *Priess, 2005*). Besides, the accurate timing of cell division and migration have been proposed to ensure the precision and robustness of cell arrangement of the whole embryo (*Fickentscher et al., 2016*; *Tian et al., 2020*). Thus, active regulations (e.g., adhesion and contraction) are usually programed to facilitate the targeted migratory cells' movement at a fixed time, resisting the unavoidable noise in cells' movements (*Marston et al., 2016*). For *C. elegans* embryo's E2 cells, which are the only precursors of gut and the first internalizing cells, a bunch of maternal and zygotic genes and proteins have been found to regulate their inward migration (*Wong et al., 2016*).

To elucidate the effect of global motional noise and local active force, we exert a white noise onto all cells' movements and a force pointing inward onto the E2 cells (see *Materials and Methods*). For each noise amplitude η ($2.5 \times 10^{-6} \sim 1.0 \times 10^{-2}$) and force intensity κ ($0 \sim 1$), the system is independently simulated for 50 times to obtain its variability in different developmental properties when the first cell internalization is completed (*Table S6*). Notably, the internalizing cells always belong to E lineage when $\eta \leq 1.0 \times 10^{-5}$, and start to be possibly derived from other lineages when $\eta > 1.0 \times 10^{-5}$; the cell type (i.e., lineage and fate) conservation decreases about 50% when η reaches 2.5×10^{-4} (*Figure 7A*). On the other hand, an active force with intensity approaching the level of intercellular repulsion (i.e., $\kappa = 1.0$) can rescue the cell type accuracy of internalizing cells to over 80% even when η reaches 1.0×10^{-2} (*Figure 7B*). In addition, compared to the non-regulated system, the ones with active force can substantially reduce the variability of the total cell number and internalizing cell number when the first internalization is activated (*Figure 7C-D*). In other words, the precision and robustness of of this morphogenetic

process can be achieved by selecting a limited set of cells for migratory control, which serves as a strategy to save system resource and improve structural accuracy during morphogenesis (*Table S6*).

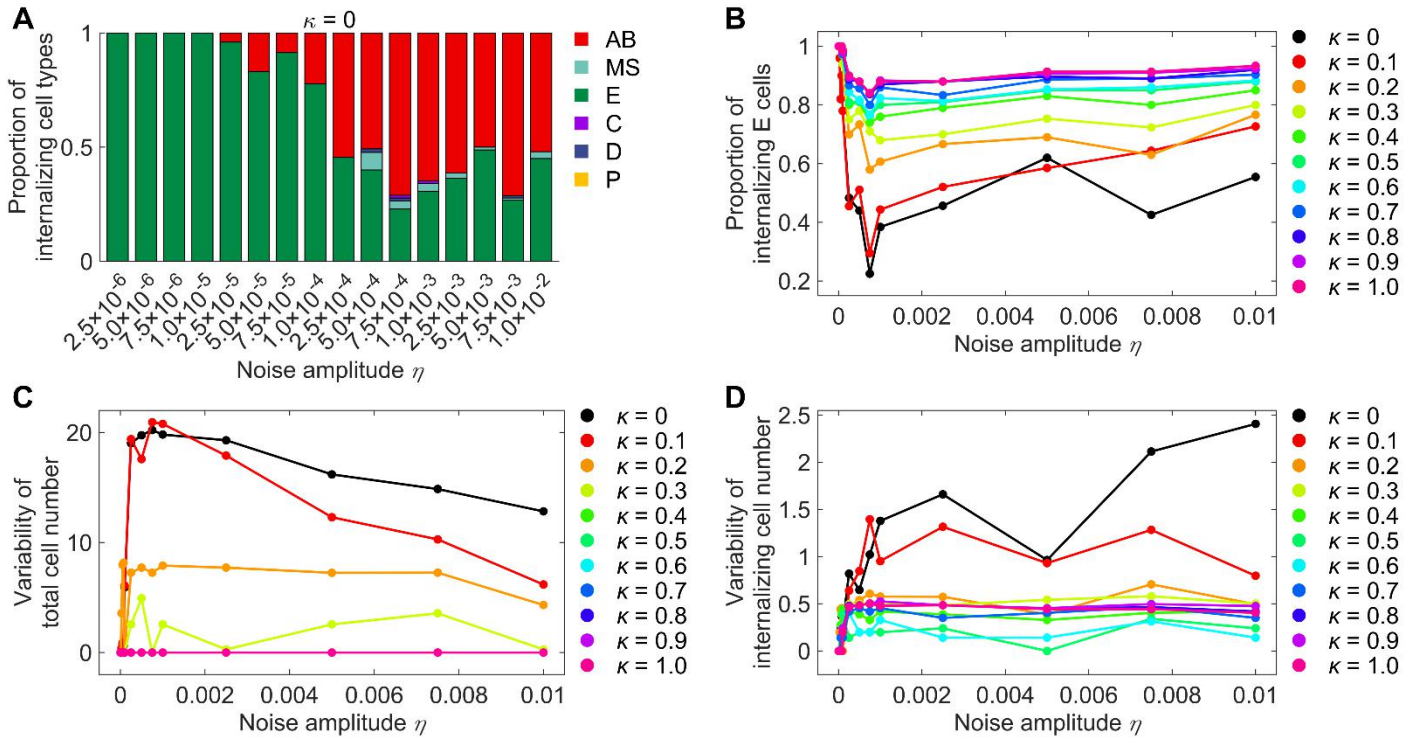

Figure 7. The simulation on the first cell internalization under different amplitude of motional noise ($\eta = 2.5 \times 10^{-6} \sim 1.0 \times 10^{-2}$) and intensity of active force ($\kappa = 0 \sim 1$). (A) Proportion of internalizing cell types when $\kappa = 0$; the relationship between colors and cell types is denoted on right. (B) Proportion of internalizing E cells. (C) Variability of total cell number. (D) Variability of internalizing cell number. The relationship between colors and κ values is denoted on the right of (B, C, D).

DISCUSSION

Cell internalization is the critical morphogenetic process for a developing embryo to generate distinct germ layers, which is extremely common among the animal kingdom. This work focuses on the well-known stereotypic developmental programs of *C. elegans* and utilizes a reductionist coarse-grained model to simulate cell-cell interaction, cell division and cell motion. We theoretically demonstrate that cell internalization can take place spontaneously in a spatially-confined proliferating blastomere, and this inevitable behavior is mainly attributed to the repulsive force from a cell's neighbors. A 2D phenomenological model, together with kinematics simulation, reveals that the cells with a large size or placed near a small-curvature boundary have a relatively higher probability to internalize. Furthermore, active regulation on specific cells' inward motion is fail-safe for such morphogenesis in all the aspects of space, time, and cell fate.

Although the intercellular force, cell size and boundary curvature are specially analyzed, other biophysical factors (e.g., embryo volume, shell shape, division orientation) plausibly influence cell internalization as well. Exemplified with the embryo volume, it's found that the total volume of cells keeps declining since gastrulation onset in the real embryo (*Figure S2A-B*). We adopt the simulation with experimental parameters, add motional noise and assign different embryo volume at the beginning. As the volume occupancy rate (embryo volume/shell volume) increases, the final number of internal cells decreases substantially (*Figure S2C* and *Table S7*). Why the embryo volume decreases over development and if it's involved with gastrulation is unclear. The potential function of such factors is worth of in-depth investigation.

The simplified model well-tuned for *C. elegans* is extensible and capable for study on other tissue- or cell-specific regulations, in addition to the E2-specific active force. In the simulation with experimental parameters and motional noise, a few of internal cells are found to move outward stochastically, severely harming the embryo's structural accuracy (*Figure S3*

and *Table S8*). Apparently, one can trap those cells inside the embryo if attraction between the internal cells is particularly strengthened in the model, and such adherence junctions have been reported to form in the intestine (*Leung et al., 1999*). Moreover, RNA interference on genes regulating cell-cell adhesion and gap junction can significantly increase the positional variability between individuals (*Li et al., 2018*). If those defects are relevant to cell internalization could also be studied with our *in silico* method.

The detailed characteristics of cell internalization discovered *in vivo* can be modeled and reexamined by our framework. For example, in the simulation with experimental parameters, we identify 35 pairs of neighboring cells which internalize one after another at a specific stage, coincidently resembling the mesendoderm internalization during zebrafish gastrulation (*Table S9*) (*Pinheiro and Heisenberg, 2020*). To distinguish if the second internalizing cell is dragged inward by first one, we remove the attractive force between them and find that all the 35 second cells can still internalize, suggesting that at least in our system, the internalization of neighboring cells are independent on each other.

How the genetic program of gastrulation is optimized during evolution is a fascinating problem that is yet to be answered. The match between *in vivo* and *in silico* cell internalization, including the activation timing, cell type and preference of cell that internalizes, indicates the underlying design logics of gastrulation programs. To sum up, our work establishes a framework to simulate cell internalization and shed light on the interpretation on worm gastrulation from mechanical perspective.

MATERIALS AND METHODS

Mechanical Model

The motion of cells is modeled within an ellipsoidal shell. The lengths of the three semi-axes of the ellipsoid are L_x = 27 μm (anterior-posterior), L_y = 18 μm (left-right) and L_z = 18 μm (dorsal-ventral), according to a recent measurement on the size of 17 *C. elegans* wild-type embryo samples (*Cao et al., 2020*). A lot of models have been proposed to reconstruct the *C. elegans* embryonic morphology *in silico*, including the multi-particle model (*Kajita et al., 2002*; *Kajita et al., 2003*), coarse-grained model (*Fickentscher et al., 2013*; *Fickentscher et al., 2016*; *Yamamoto and Kimura, 2017*; *Tian et al., 2020*; *Guan et al., 2020*), deep-learning model (*Wang et al., 2018*; *Wang et al., 2019*) and phase field model (*Jiang et al., 2019*; *Kuang et al., 2020*). Among them, the coarse-grained ones have shown great advantage in scaling up of cell number and capturing interpretable characteristics of morphogenetic dynamics.

Here, we follow the previous work which improved the coarse-grained model by optimizing the system parameters using *in vivo* embryo morphology data (*Guan et al., 2020*). The pressure exerted on a cell from the shell is given by

$$\boldsymbol{F}_{shell\to i} = k_{shell}\boldsymbol{e}_{shell\to i}\cdot\begin{cases} R_i - d_i, & 0 < d_i \le R_i \\ 0, & d_i > R_i \end{cases} \tag{1}$$

where k_{shell} is the elastic coefficient representing the intensity of cell-shell repulsion; $\boldsymbol{e}_{shell\to i}$ is the direction vector orienting from the shell (contact point) to cell i; d_i is the minimal distance between them; R_i is the radius of cell i. Apart, the interaction between cells combines both repulsion (volume effect when r_{ij} is small) and attraction (membrane adhesion when r_{ij} is large). For simplicity, the interaction is described as linear functions controlled by the mean radius of cell i and cell j,

$$\boldsymbol{F}_{j\to i} = \frac{F_{cell}}{2\alpha\overline{R}_{ij}}\boldsymbol{e}_{j\to i}\cdot\begin{cases} 2\alpha\overline{R}_{ij} - r_{ij}, & 0 < r_{ij} \le (1+\alpha)\overline{R}_{ij} \\ r_{ij} - 2\overline{R}_{ij}, & (1+\alpha)\overline{R}_{ij} < r_{ij} \le 2\overline{R}_{ij} \\ 0, & r_{ij} > 2\overline{R}_{ij} \end{cases} \tag{2}$$

where $F_{cell} = k_{shell}K$ represents intercellular elastic capacity with k_{shell} as unit; $\boldsymbol{e}_{j\to i}$ is the direction vector orienting from cell j to cell i; $\overline{R}_{ij}$ is the mean radius of cell i and cell j; α determines the range of repulsive force. $K = 0.01$ μm and $\alpha = 0.9$ have been found to be optimal for *C. elegans* embryo during 4- to ~50-cell stage. It's worth pointing out that, only the cells identified as Voronoi neighbors are taken into account.

Since the environment inside the shell is highly viscous, the motion of a cell can be described by an overdamped Langevin

equation (***Fickentscher et al., 2013***),

$$\zeta \frac{\mathrm{d}\boldsymbol{r}_i}{\mathrm{d}t} = \boldsymbol{F}_{shell\to i} + \sum_{\boldsymbol{j}} \boldsymbol{F}_{j\to i} + \boldsymbol{f}_i \tag{3}$$

Here, ζ is the viscosity coefficient; $\boldsymbol{r}_i$ is the position vector of cell i; $\boldsymbol{f}_i$ is the random force with a mean $\langle \boldsymbol{f}_i \rangle = 0$ and a variance $\langle \boldsymbol{f}_i(t)\boldsymbol{f}_j(t') \rangle = M\delta_{ij}\delta(t-t')$, where M is the noise amplitude, δ_{ij} is the Kronecker delta function, and $\delta(t-t')$ is the Dirac delta function. The discrete form of ***Equation 3*** reads

$$\boldsymbol{r}_i(t+\Delta t) = \boldsymbol{r}_i(t) + \Delta t[\boldsymbol{F}_{shell\to i}(t) + \sum_{\boldsymbol{j}} \boldsymbol{F}_{j\to i}(t)] + \sqrt{\Delta t}\eta\boldsymbol{\xi} \tag{4}$$

where $\eta = \sqrt{\frac{M}{\zeta}}$ is the equivalent noise amplitude and $\boldsymbol{\xi}$ is a three-dimensional random variable obeying the standard normal distribution.

When it comes to the investigation on active migratory regulation, an active force toward the inner side of the shell is exerted onto the Ea and Ep cells since 26-cell stage to facilitate their internalization, which is expressed by

$$\boldsymbol{F}_{active} = \kappa F_{cell}\left(2 - \frac{d_i}{R_i}\right)\boldsymbol{e}_{shell\to i},\ 0 < d_i \le 2R_i \tag{5}$$

where κ represents the intensity of active force.

The simulation is performed from 4- to 330-cell stage in accordance to the highly conserved cell division sequence (27 groups of division events in total) obtained from *in vivo* experiments (***Table S2***) (***Guan et al., 2019***). The configuration of the first 4 cells (i.e., ABa, ABp, EMS and P2) is initialized as the well-known rhombic pattern (***Yamamoto and Kimura, 2017***). All the cells are assumed to undergo symmetric divisions except the P lineages (i.e., P0, P1, P2 and P3), whose volume segregation ratios are assigned based on experimental measurement. The volume segregation ratios of P0, P1, P2, P3 are 1.324, 1.557, 2.045, and 2.364, respectively, while the final P cell, P4, is set to divide equally to generate the germ-line percussors Z2 and Z3, which keep arrested until larva stage. The division event is approximated by replacing each dividing cell by two daughter cells positioned along the prescribed division orientation, which have an initial distance of 1.16 times of the radius of mother cell (D_{sister} / R_{mother} = 1.16; ***Figure S4***). All the volume and distance ratios are obtained from the experimental data of 17 segmented *C. elegans* wild-type embryo samples collected in ***Cao et al., 2020***. Each group of division events are activated when the whole system's motion perturbed by the previous division events reaches equilibrium, in other words, its mean kinetic energy is close to the fluctuation energy associated with the intrinsic noise:

$$\sum_{j=1}^{N_{step}}\sum_{i=1}^{N}\left|\frac{\boldsymbol{r}_i(t_j+\Delta t)-\boldsymbol{r}_i(t_j)}{\Delta t}\right|^2/2/N/N_{step} < 10^{-8} + \frac{3\eta^2}{2\Delta t} \tag{5}$$

where N is the total cell number; $N_{step} = 600000$ is the inspected time step number; Δt is the time step and chosen to be 0.1; $\frac{3\eta^2}{2\Delta t}$ represents the fluctuation energy of stochastic motion and the small amount 10^{-8} demands the system approaching equilibrium with very little additional energy.

Division Orientation

The orientation of cell division is autonomous and set by the following rules:

1. As a default, a cell lying at the position $P(x, y, z)$ divides along the direction vector $\boldsymbol{e}_{division} = (y\Delta_y + z\Delta_z,\ -y\Delta_x,\ -z\Delta_x)$, where $\boldsymbol{e}_{outward} = (\Delta_x, \Delta_y, \Delta_z)$ is the vector orienting from the position *P* to the point of the shell that is the closest to *P*. Geometrically, $\boldsymbol{e}_{division}$ is perpendicular to $\boldsymbol{e}_{outward}$ and located in a plane overlapping the *x* axis. This quantitative rule can resemble the actual cell division behaviors in which most division axes are near the anterior-posterior axis and tangent to the shell.

   Several exceptions are listed below to prevent the potential problems in cell identification and structural bifurcation during simulation:

2. When a cell lies nearby the *x* axis (with a distance to the *x* axis less than 0.2 times of the cell radius) but off the anterior and posterior terminal (with a distance to the shell longer than 1.2 times the cell radius), it divides along the direction vector $\boldsymbol{e}_x$.
3. When a cell lies nearby the *x* axis and around the anterior or posterior terminal (with a distance to the shell no longer than 1.2 times the radius of the cell), it divides along the direction vector $0.100\boldsymbol{e}_x - 0.995\boldsymbol{e}_z$.
4. Since the cells ABa and ABp in the wild-type embryos divide approximately along the left-right axis (*y*), violating the default above, extra clockwise rotations of 45° are performed on their division orientations and the rotation axes are set as $-\boldsymbol{e}_x$ and $\boldsymbol{e}_z$ for ABa and ABp, respectively.

Cell Identification

The cell identity/name is determined by its mother's division orientation in accordance to the nomenclature in *C. elegans* embryogenesis research (***Sulston et al., 1983***). Generally, for the symmetric division of a cell *X*, the two daughters are named as *X*a (closer to $-e_x$) and *X*p (closer to e_x). Note that there are three exceptions: (1) for the germline stem cell divisions, P0, P1, P2, P3, P4's daughters are named as P1, P2, P3, P4, Z3 (closer to e_x) and AB, EMS, C, D, Z2 (closer to $-e_x$), respectively. (2) for the ABa and ABp cells, the daughters are named as *X*l (closer to $-e_y$) and *X*r (closer to e_y); (3) for the EMS cell, the daughters are named as E (closer to e_x) and MS (closer to $-e_x$).

ACKNOWLEDGMENTS

We thank Siyu Chen, Prof. Xiaojing Yang and the members of Tang Lab for helpful discussions and comments. This work was supported by the National Natural Science Foundation of China (Grant Nos. 12090053, 32088101). Part of the computation was carried out on the High-Performance Computing Platform of the Center for Life Sciences, Peking University.

COMPETING INTERESTS

The authors declare that no competing interests exist.

AUTHOR ORCIDS

Jiao Miao, https://orcid.org/0000-0003-3097-1281

Guoye Guan, https://orcid.org/0000-0003-4479-4722

Chao Tang, https://orcid.org/0000-0003-1474-3705

AUTHOR CONTRIBUTIONS

Jiao Miao, Guoye Guan, Conceptualization , Data curation, Formal analysis, Investigation, Visualization, Modeling, Writing - original draft; Chao Tang, Conceptualization, Resources, Formal analysis, Supervision, Funding acquisition, Validation, Methodology, Writing - original draft, Project administration.

REFERENCES

Dehaan RL, Ebert JD. 1964. Morphogenesis. *Annual Review of Physiology* **26**:15-46. DOI: https://doi.org/10.1146/annurev.ph.26.030164.000311

Kumar M, Pushpa K, Mylavarapu SVS. 2015. Splitting the cell, building the organism: mechanisms of cell division in metazoan embryos. *IUBMB Life* **67**:575-587. DOI: https://doi.org/10.1002/iub.1404

Farrell JA, Wang Y, Riesenfeld SJ, Shekhar K, Regev A, Schier AF. 2018. Single-cell reconstruction of developmental trajectories during zebrafish embryogenesis. *Science* **360**:eaar3131. DOI: https://doi.org/10.1126/science.aar3131, PMID: 29700225

Packer JS, Zhu Q, Huynh C, Sivaramakrishnan P, Preston E, Dueck H, Stefanik D, Tan K, Trapnell C, Kim J, Waterston RH, Murray JI. 2019. A lineage-resolved molecular atlas of *C. elegans* embryogenesis at single-cell resolution. *Science* **365**:eaax1971. DOI: https://doi.org/10.1126/science.aax1971, PMID: 31488706

Stern CD. 2004. Gastrulation: from cells to embryo. Cold Spring Harbor Laboratory Press. URL: www.gastrulation.org

Solnica-Krezel L, Sepich DS. 2012. Gastrulation: making and shaping germ layers. *Annual Review of Cell and Developmental Biology* **28**:687-717. DOI: https://doi.org/10.1146/annurev-cellbio-092910-154043

Houthoofd W, Willems M, Vangestel S, Mertens C, Bert W, Borgonie G. 2006. Different roads to form the same gut in nematodes. *Evolution & Development* **8**:362-369. DOI: https://doi.org/10.1111/j.1525-142X.2006.00108.x, PMID: 16805900

Swalla BJ. 1993. Mechanisms of gastrulation and tail formation in ascidians. *Microscopy Research and Technique* **26:**274-284. DOI: https://doi.org/10.1002/jemt.1070260403, PMID: 8305720

Lemke S, Kale G, Urbansky S. 2015. Comparing gastrulation in flies: Links between cell biology and the evolution of embryonic morphogenesis. *Mechanism of Development* **164**:103648. DOI: https://doi.org/10.1016/j.mod.2020.103648

Heasman J. 2006. Patterning the early *Xenopus* embryo. *Development* **133**:1205-1217. DOI: https://doi.org/10.1242/dev.02304

Rohde LA, Heisenberg CP. 2007. Zebrafish gastrulation: cell movements, signals, and mechanisms. *International Review of Cytology* **261**:159-192. DOI: https://doi.org/10.1016/S0074-7696(07)61004-3, PMID: 17560282

Chapman SC, Schubert FR, Schoenwolf GC, Lumsden A. 2002. Analysis of spatial and temporal gene expression patterns in blastula and gastrula stage chick embryos. *Developmental Biology* **245**:187-199. DOI: https://doi.org/10.1006/dbio.2002.0641, PMID: 11969265

Tam PPL, Behringer RR. 1997. Mouse gastrulation: the formation of a mammalian body plan. *Mechanisms of Development* **68**:3-25. DOI: https://doi.org/10.1016/S0925-4773(97)00123-8

Ghimire S, Mantziou V, Moris N, Arias AM. 2021. Human gastrulation: the embryo and its models. *Developmental Biology* **474**:100-108. DOI: https://doi.org/ 10.1016/j.ydbio.2021.01.006, PMID: 33484705

Vicente C. 2015. An interview with Lewis Wolpert. *Development* **142**:2547-2548. DOI: https://doi.org/10.1242/dev.127373, PMID: 26243866

Illman J. 2021. Lewis Wolpert: developmental biologist who raised the public profile of mental illness. *BMJ* **372**:n441. DOI: https://doi.org/10.1136/bmj.n441

Corsi AK, Wightman B, Chalfie M. 2015. A transparent window into biology: a primer on *Caenorhabditis elegans* (June 18, 2015). *WormBook*. DOI: https://doi/10.1895/wormbook.1.177.1, PMID: 26088431

Nance J, Lee JY, Goldstein B. 2005. Gastrulation in *C. elegans* (September 26, 2005). *WormBook*. DOI: https://doi/10.1895/wormbook.1.23.1, PMID: 18050409

Goldstein B, Nance J. 2020. *Caenorhabditis elegans* gastrulation: a model for understanding how cells polarize, change shape, and journey toward the center of an embryo. *Genetics* **214**:265-277. DOI: https://doi.org/ 10.1534/genetics.119.300240

Chisholm AD, Hardin J. 2005. Epidermal morphogenesis (December 01, 2005). *WormBook*. DOI: https://doi/10.1895/wormbook.1.35.1, PMID: 18050408

Nance J, Priess JR. 2002. Cell polarity and gastrulation in *C. elegans*. *Development* **129**:387-397. PMID: 11807031

Marston DJ, Higgins CD, Peters KA, Cupp TD, Dickinson DJ, Pani AM, Moore RP, Cox AH, Kiehart DP, Goldstein B. 2016. MRCK-1 drives apical constriction in *C. elegans* by linking developmental patterning to force generation. *Current Biology* **26**:2079-2089. DOI: https://doi/10.1016/j.cub.2016.06.010, PMID: 27451898

Cao J, Guan G, Ho VWS, Wong MK, Chan LY, Tang C, Zhao Z, Yan H. 2020. Establishment of a morphological atlas of the *Caenorhabditis elegans* embryo using deep-learning-based 4D segmentation. *Nature Communications* **11**:6254. DOI: https://doi.org/10.1038/s41467-020-19863-x, PMID: 33288755

Fickentscher R, Struntz P, Weiss M. 2013. Mechanical cues in the early embryogenesis of *Caenorhabditis elegans*. *Biophysical Journal* **105**:1805-1811. DOI: https://doi.org/10.1016/j.bpj.2013.09.005, PMID: 24138856

Fickentscher R, Struntz P, Weiss, M. 2016. Setting the clock for fail-safe early embryogenesis. *Physical Review Letters* **117**:188101. DOI: https://doi.org/10.1103/PhysRevLett.117.188101, PMID: 27835015

Yamamoto K, Kimura A. 2017. An asymmetric attraction model for the diversity and robustness of cell arrangement in nematodes. *Development* **144**:4437-4449. DOI: https://doi.org/10.1242/dev.154609, PMID: 29183946

Tian B, Guan G, Tang LH, Tang C. 2020. Why and how the nematode's early embryogenesis can be precise and robust: a mechanical perspective. *Physical Biology* **17**:026001. DOI: https://doi.org/10.1088/1478-3975/ab6356, PMID: 31851962

Guan G, Tang LH, Tang C. 2020. Reconstructing the multicellular structure of a developing metazoan embryo with repulsion-attraction model and cell-cell connection atlas *in vivo*. *Journal of Physics: Conference Series* **1592**:012020. DOI: https://doi.org/10.1088/1742-6596/1592/1/012020

Sugioka K, Bowerman B. 2018. Combinatorial contact cues specify cell division orientation by directing cortical myosin flows. *Developmental Cell* **46**:257-270. DOI: https://doi.org/10.1016/j.devcel.2018.06.020, PMID: 30032990

Guan G, Wong MK, Ho VWS, An X, Chan LY, Tian B, Li Z, Tang LH, Zhao Z, Tang C. 2019. System-level quantification and phenotyping of early embryonic morphogenesis of *Caenorhabditis elegans*. *bioRxiv* 776062, preprint at https://www.biorxiv.org/content/10.1101/776062v1

Simonsen KT, Moerman DG, Naus CC. 2014. Gap junctions in *C. elegans*. *Frontiers in Physiology* **5**:40. DOI: https://doi.org/10.3389/fphys.2014.00040, PMID: 24575048

Pegoraro AF, Janmey P, Weitz DA. 2017. Mechanical properties of the cytoskeleton and cells. *Cold Spring Harbor Perspectives in Biology* **9**:a022038. DOI: https://doi.org/10.1101/cshperspect.a022038, PMID: 29092896

Li X, Zhao Z, Xu W, Fan R, Xiao L, Ma X, Du Z. 2018. Systems properties and spatiotemporal regulation of cell position variability during embryogenesis. *Cell Reports* **26**:313-321. DOI: https://doi.org/10.1016/j.celrep.2018.12.052, PMID: 30625313

Eisenmann DM. 2005. Wnt signaling (June 25, 2005). *WormBook*. DOI: https://doi/10.1895/wormbook.1.7.1

Priess J. 2005. Notch signaling in the *C. elegans* embryo (June 25, 2005). *WormBook*. DOI: https://doi.org/10.1895/wormbook.1.4.1

Wong MK, Guan D, Ng KHC, Ho VWS, An X, Li R, Ren X, Zhao Z. 2016. Timing of tissue-specific cell division requires a differential onset of zygotic transcription during metazoan embryogenesis. *Journal of Biological Chemistry* **291**:12501-12513. DOI: https://doi.org/10.1074/jbc.M115.705426, PMID: 27056332

Harrell JR, Goldstein B. 2011. Internalization of multiple cells during *C. elegans* gastrulation depends on common cytoskeletal mechanisms but different cell polarity and cell fate regulators. *Developmental Biology* **350**:1-12. DOI: https://doi.org/10.1016/j.ydbio.2010.09.012, PMID: 20875815

Leung B, Hermann GJ, Priess JR. 1999. Organogenesis of the *Caenorhabditis elegans* intestine. *Developmental Biology* **216**:114-134. DOI: https://doi.org/10.1006/dbio.1999.9471, PMID: 10588867

Pinheiro D, Heisenberg CP. 2020. Zebrafish gastrulation: Putting fate in motion. *Current Topics in Developmental Biology* **136**:343-375. DOI: https://doi.org/10.1016/bs.ctdb.2019.10.009, PMID: 31959295

Kajita A, Yamamura M, Kohara Y. 2002. Physical modeling of the cellular arrangement in *C. elegans* early embryo: effect of rounding and stiffening of the cells. *Genome Informatics* **13**:224-232.

Kajita A, Yamamura M, Kohara Y. 2003. Computer simulation of the cellular arrangement using physical model in early cleavage of the nematode *Caenorhabditis elegans*. *Bioinformatics* **19**:704-716. DOI:

https://doi.org/10.1093/bioinformatics/btg069, PMID: 12691982

Wang Z, Wang D, Li C, Xu Y, Li H, Bao Z. 2018. Deep reinforcement learning of cell movement in the early stage of *C. elegans* embryogenesis. *Bioinformatics* **34**:3169-3177. DOI: https://doi.org/10.1093/bioinformatics/bty323, PMID: 29701853

Wang Z, Wang D, Li C, Xu Y, Li H, Bao Z. 2019. Modeling cell migration with convolutional neural network and deep reinforcement learning. *Workshop on Computational Biology at the International Conference on Machine Learning*, https://www.osti.gov/servlets/purl/1543193.

Jiang J, Garikipati K, Rudraraju S. 2019. A diffuse interface framework for modeling the evolution of multi-cell aggregates as a soft packing problem driven by the growth and division of cells. *Bulletin of Mathematical Biology* **81**:3282-3300. DOI: https://doi.org/10.1007/s11538-019-00577-1, PMID: 30778833

Kuang X, Guan G, Wong MK, Chan LY, Zhao Z, Tang C, Zhang L. 2020. Computable early *C. elegans* embryo with a data-driven phase field model. *bioRxiv* 422560, preprint at https://www.biorxiv.org/content/10.1101/2020.12.13.422560v2